Krishnan *et al. Journal of Electric Propulsion* (2026) 5:12
https://doi.org/10.1007/s44205-026-00189-7

Journal of Electric Propulsion

RESEARCH **Open Access**

Correlation and causation and time-lagged phase portrait analysis of discharge current and plume ion flux in a hall thruster as a function of facility operating pressure

Ajay Krishnan[1,2*], Naia Butler-Craig[1,3], Dan Lev[1,3] and Mitchell L. R. Walker[1,3]

*Correspondence:
Ajay Krishnan
ajaykrishnan@gatech.edu
[1]Georgia Institute of Technology, Atlanta, GA 30332, USA
[2]School of Electrical and Computer Engineering, USA, 777 Atlantic Drive NW, Atlanta, GA 30332, USA
[3]School of Aerospace Engineering, 270 Ferst Drive, Atlanta, GA 30332, USA

Abstract

We characterize discharge current and plume ion flux oscillations of the H9 Hall effect thruster (HET) at the 6-kW, 300 V, and 20 A operating condition, using krypton propellant. Initial time and frequency domain analyses show similarities between discharge current and ion flux. We then use the extended convergent cross mapping (eCCM) technique to validate the discharge current and ion flux dataset by determining their correlation and causation at background vacuum chamber pressures of 6.236, 14.03, 21.83, 28.06, 32.74, and 38.98 μTorr-Kr. We construct time-lagged phase portraits (TLPPs) to provide a unique representation of the H9 HET as a function of the operating pressure and to assess the similarity between discharge current and ion flux. The results show a high, positive correlation between discharge current and ion flux that decreases with increasing operating pressure, with a maximum correlation of 0.9547. Additionally, the discharge current influences the ion flux; this observation matches what one would expect, as ion flux originates within the thruster cavity where electron density oscillations are generated. The correlation results show that the eCCM technique can determine causality in thruster measurements. Furthermore, the TLPPs represent a fingerprint of a HET that can allow one to determine the operating state of the thruster as a function of operating pressure using the Earth mover's distance (EMD) metric. From the lowest pressure, used as the reference, to the highest pressure, the EMD values are 0, 1.092, 1.672, 1.753, 1.871, and 2.023, showing that each TLPP is indeed distinct.

Keywords Pressure facility effects, Discharge current oscillations, Ion flux oscillations, eCCM, Phase portraits, H9 Hall Thruster

Introduction

A Hall effect thruster (HET) is an electrostatic plasma device that produces thrust via the acceleration of ions [1]. They were first developed in the 1960s and have since been increasingly adopted as propulsion systems for spacecraft due to their high specific impulse as compared to chemical propulsion systems [1, 2]. The development of such propulsion technology requires operating HETs in dedicated ground-based vacuum chambers that replicate conditions as close as possible to those expected in space. However, it is not possible to fully emulate space conditions on the ground, leading to unintended deviations from the performance and physics as measured in space [3].

The use of vacuum chambers introduces what are referred to as facility effects, changes to HET performance, plume, and discharge physics on the ground compared to those in space [3]. Facility effects occur because of three distinct features of the vacuum chamber. First, pressure facility effects are the result of a vacuum chamber pumping system's inability to reach the low-pressure levels as in space [4]. Second, the existence of a large metal facility creates current paths that otherwise do not exist in the space environment [5–7]. Third, the sputtering of material from the chamber walls back onto and into the HET may interfere with the discharge and affect thruster lifetime [3]. Thus, it is necessary to understand the influence of different facility effects on HET physics and operation and to quantify when a HET operated in a vacuum chamber has the same operating mode as a HET in space. In this study, we specifically focus on pressure facility effects.

Pressure facility effects have been shown to have an impact on the oscillatory behavior of a HET, but we will first discuss the origin of the so-called "breathing mode" oscillations (BMOs) [7]. BMOs are the result of plasma instabilities in the discharge of a HET [8]. Of the various types of HET oscillations, BMOs are the predominant type and are tied to predator-prey interactions between neutrals and electrons in the discharge chamber plasma. The BMOs create variations in plasma parameters, specifically plasma density, in the discharge chamber of the thruster. The dynamics of the BMOs can be expressed by the conservation of mass, momentum, and energy Eq [9]. This dominant mode occurs in the tens of kHz range and can lead to discharge current amplitudes of over 100% of the mean [10]. It plays a significant role in the dynamics and performance of a HET, as highly oscillatory thrusters show degraded performance. Discharge current flows out through the plume, which contains an ion flux component that is also oscillatory due to ion density oscillations in the plume [11]. The ion flux can be measured with plasma diagnostics, such as a Faraday probe [12]. Having discussed BMO, we now return to discussing operating pressure effects.

Several studies have characterized the effects of operating pressure on HET discharge oscillations [13, 14]. Some have found that increasing operating pressure increases the amplitude of discharge oscillations and increases thrust. Furthermore, increasing operating pressure shifts the location of the ionization region upstream and changes ion energy [13, 14]. The relationship between discharge current and operating pressure must be understood to predict the oscillations that would occur in space. It can be observed that facility effects no longer change HET performance as operating pressure decreases and approaches the vacuum conditions of space [3]. An important first step before proceeding with the experimental collection of a dataset that investigates the relationship between operating pressure, discharge current, and ion flux is to validate it. Our approach to validation consists of determining correlation and causation; the discharge current should cause the observed ion flux at the selected operating pressure. Beyond validation of experimental conditions, an investigation of how operating pressure affects the correlation between discharge current and ion flux can provide insight into plasma dynamics from the HET into its plume.

We choose the discharge current and ion flux signals because their expected relationship is known, aiding in the correlation validation process. Note that no prior studies have investigated the correlation between ion flux in the thruster plume and discharge current at various operating pressures. An experiment is devised to determine the correlation and causation between discharge current and ion flux at different operating pressures. Determining causality in a nonlinear and time-varying system such as a HET can be accomplished using convergent cross mapping (CCM), a technique based on Takens' Theorem, and using shadow manifolds [15]. Shadow manifolds are the result of projecting a system's signals onto coordinate axes that are time-lagged. The basis is that if a signal causes another signal, then the signal is recorded in the other signal. The extended convergent cross mapping (eCCM) technique allows for the determination of causal links between HET measurements [16]. eCCM allows one to see which parameter affects the other and how strongly it affects it as well. For signal X to cause signal Y, X should cross-map Y for positive X to Y time shifts, while Y should cross-map X for negative time shifts. For causation and correlation to appear, there should be characteristic peaks in the plots that are shifted from one another. Huerta et al.. at the Air Force Research Laboratory (AFRL) have successfully developed and used the eCCM technique to determine causality from a variety of measurements obtained between two different plasma probes and between the discharge current and a single plasma probe [15, 16]. They used eCCM to show that discharge current causes ion flux, in other words that ion flux originates from the discharge current, but they did not investigate the effects of varying the background pressure.

After dataset validation, we turn our attention to analyzing the dynamics of discharge current and ion flux oscillations. Time-lagged phase portraits (TLPPs) of the discharge current and ion flux provide a unique representation of a HET, dependent on the operating point (discharge voltage, mass flow rate and magnetic field) and on the operating conditions, e.g., background pressure, allowing one to create a fingerprint of a HET operating at a particular condition [17]. TLPPs are created by plotting a signal against a shifted version of itself, leading to a more compact version of the time domain signal with key features that help identify the phase portraits from others. Probability density functions (PDFs) can be combined with TLPPs to create PDF-TLPPs, which represent color intensity plots that depict the statistics of the TLPP, particularly where the TLPP data is most strongly present. One could potentially determine what facility, thruster, propellant, and operating conditions were used from a phase portrait. Having identical phase portraits from multiple thrusters operating under different settings could mean that the thrusters exhibit the same performance. The Earth mover's distance (EMD) metric, which represents how much matter must be moved to make one TLPP the same as another, is often used for analyzing TLPPs. Presently, no prior studies have constructed phase portraits at varying operating pressures. Doing so would allow one to see whether pressure facility effects are still present in the testing facility. Thus, we create TLPPs and analyze their EMDs to examine thruster operating states at different background pressures.

This paper presents an experimental effort to determine the influence of operating pressure on the correlation between discharge current and ion flux in the plume of a 9-kW HET. Section "Experimental" presents the experimental setup used to conduct testing. Section "Results and discussion" describes the methods used to perform testing and analyze the results. Section "Conclusion" presents the results, and the remaining sections discuss the results and their implications. The discussion presents three distinct contributions related to the correlation and causation between discharge current and ion flux and their TLPP representations. One, we show that the similarity in the time and frequency domains of discharge current and ion flux varies with operating pressure by providing relevant plots that illustrate this finding. Two, we show that discharge current and ion flux are correlated and that discharge current causes ion flux at six different operating pressures by using correlation versus time-shift plots generated by the eCCM algorithm. Three, we outline the use of TLPPs to represent various thruster modes and determine if thrusters operate in the same way in different environments by generating TLPPs for discharge current and ion flux at each of the six operating pressures and their corresponding EMDs.

Experimental

Section A discusses the vacuum test facility used to conduct experimentation on the HET. Section B discusses the specific thruster used, the H9 HET. Section C discusses pressure diagnostics used to determine operating pressure and the plasma diagnostics that were used to measure ion flux in the plume. Section D discusses the operating conditions of the H9 thruster. These include the six operating pressures along with the voltage, current, flow rates, and magnet current settings. Six pressure conditions were chosen to sufficiently illustrate how the phase portraits and the results of the eCCM algorithm change. Section E discusses data collection procedures, which involve using a Faraday probe, while section F discusses the eCCM technique in addition to the post-processing of the data. These post-processing techniques include generating correlation-time shift plots and phase portraits, which demonstrate the effectiveness of the eCCM algorithm and provide a more compact representation of discharge oscillations. Lastly, section G discusses uncertainty quantification for this study.

Vacuum facility

All experiments are performed in Vacuum Test Facility 2 (VTF-2) at the Georgia Institute of Technology High-Power Electric Propulsion Laboratory (HPEPL). Figure 1 shows a schematic of this facility. VTF-2 is a stainless-steel chamber measuring 9.2 m in length and 4.9 m in diameter. VTF-2 is evacuated to a rough vacuum using one 495 CFM rotary-vane pump and one 3800 CFM blower. High vacuum of 5.5×10^{-9} Torr is achieved using ten liquid nitrogen-cooled CVI TMI re-entrant cryopumps at a pumping speed of 350,000 l/s on xenon. The cryopump shrouds are fed using the Stirling Cryogenics SPC-8 RL special closed-loop nitrogen liquefaction system [4].

H9 HET setup and operation

For this study, we use the H9 HET, a 9-kW class magnetically shielded HET developed in partnership between the University of Michigan, the Jet Propulsion Laboratory (JPL), and the AFRL [18]. The H9 employs a centrally-mounted LaB_6 cathode. The performance of the H9 has been extensively mapped on krypton through prior investigations [19]. The thruster body is isolated from facility ground and the cathode common is electrically floating. Thruster body isolation is achieved via ceramic standoffs that isolate the thruster body from its support structures.

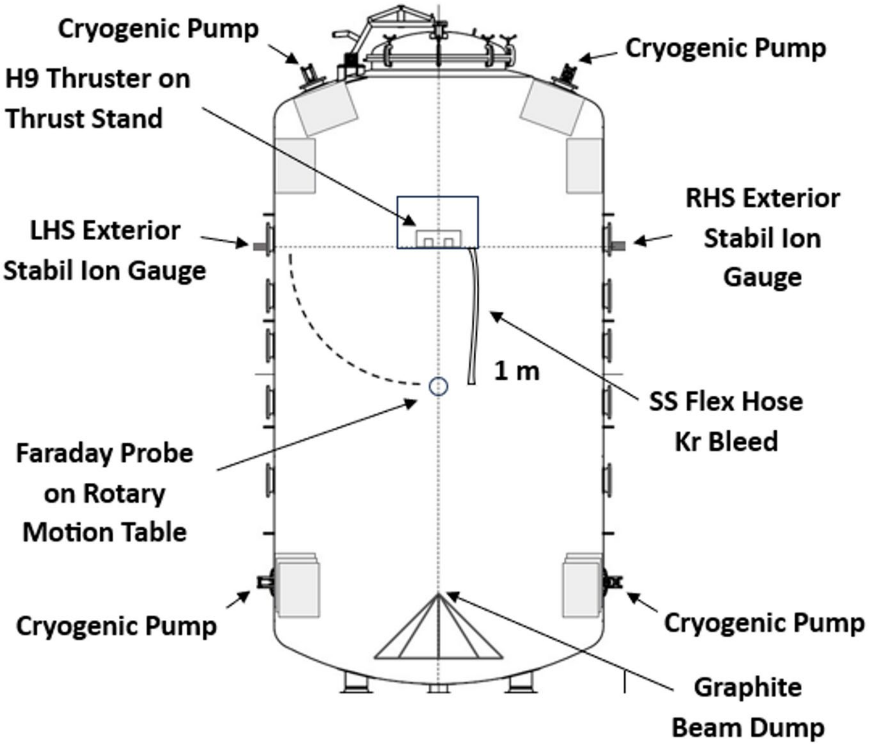

Fig. 1 VTF-2 layout

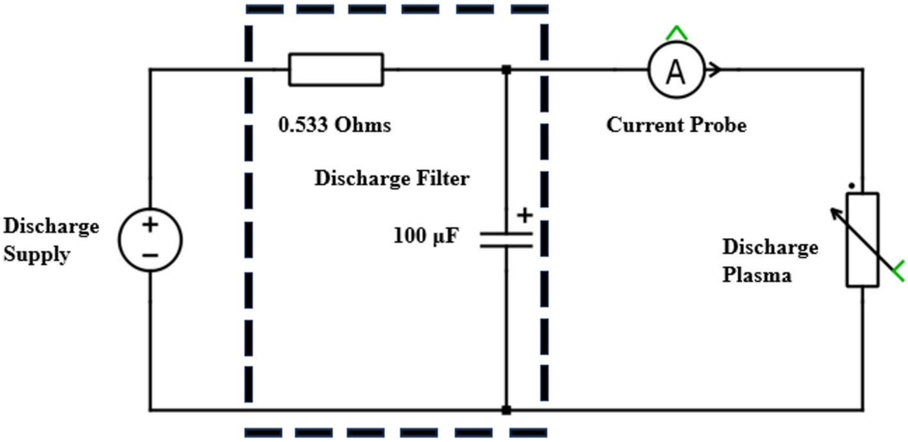

Fig. 2 Discharge circuit with current probe

The H9 discharge was controlled using a Magna-Power TSA800-54 power supply. The inner and outer magnets were powered using TDK-Lambda GEN80-42 power supplies. A TDK-Lambda GEN600-2.6 and GEN60-25 are used for the cathode keeper and heater, respectively. To protect the discharge supply from thruster oscillations, the discharge supply is connected to a low-pass discharge filter consisting of a series 0.533-Ω resistor and a shunt 100-μF capacitor to attenuate discharge current oscillations that are greater than 3 kHz in frequency. Figure 2 shows the electrical diagram of the discharge circuit.

High-purity (99.999%) krypton propellant is supplied to the anode, cathode, and bleed line using stainless-steel lines metered with MKS GE50A mass flow controllers (MFCs). The MFCs are calibrated with a MesaLabs DryCal 800 – 10 volumetric flow meter. The uncertainty for the anode, cathode, and bleed lines are 2%, 5%, and 2%, respectively. Operating pressures of 6.236, 14.03, 21.83, 28.06, 32.74, and 38.98 μTorr-Kr are set using the bleed flow, which is stabilized in less than five minutes.

Pressure and plasma diagnostics

Pressure in VTF-2 is monitored using Stabil Ion ionization gauges with an accuracy of ± 4%, controlled by an Agilent XGS-600 Gauge Controller. Gauges can be mounted to flanges on both sides of the chamber's exterior, though only the ion gauge mounted on the right-hand side of the chamber was used. Pressure measurements are corrected for krypton gas using a gas correction factor for the gauge controller.

The ion flux in the thruster plume is measured using a Faraday probe. The Faraday probe is a well-known diagnostic tool that uses an electrostatically biased collector plate to repel electrons and collect ions [12]. The Faraday probe used has a collector plate area of 3.87 cm^2, with 1.1% uncertainty. Past studies show that the maximum current density obtained using the Faraday probe is 40 A/m^2 [19]. Figure 3 shows the Faraday probe electrical schematic. A fixed − 30 V bias is applied between the collector and guard terminals of the Faraday probe, creating electron current that matches ion current. A 68 Ω resistor with 5% uncertainty is used as a current shunt. The voltage drop across the current shunt can be used to determine the ion current via Ohm's law and can subsequently be converted to ion flux. Faraday probe data were collected on the thruster centerline, 1 m downstream from the exit plane of the H9 thruster. A rotary arm moves the attached Faraday probe from the side of the HET to the centerline, where simultaneous ion current and discharge current measurements are recorded, after which the rotary arm is then immediately moved to the side of the thruster to not damage the Faraday probe. The magnitude uncertainty of the Faraday probe measurement is 5.22%, while the timing uncertainty is on the nanosecond order of magnitude.

Thruster operation

Table 1 shows the operating conditions that were used for the H9 HET during experimentation. The power supply voltage, anode and cathode flow rate, and the magnetic field remain constant during testing. The thruster is operated for three hours until its oscillations become steady, where the average discharge current varies less than 1% throughout testing. Six pressure conditions are selected, the first being at ambient conditions with no additional injection of krypton, and the remaining five spanning the pressure range up to 40 μTorr. A discharge voltage of 300 V and a mean discharge current of

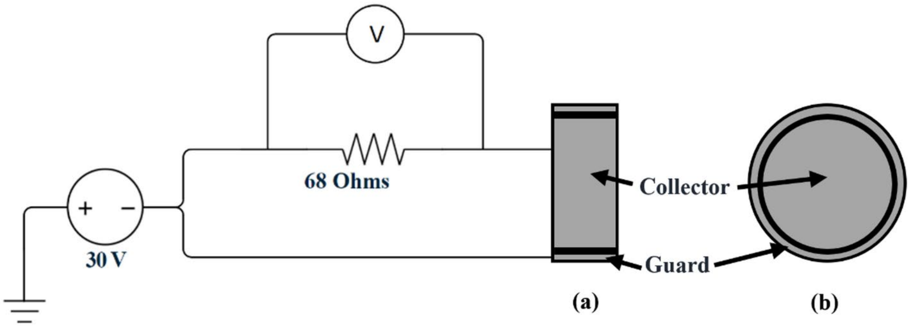

Fig. 3 Faraday probe electrical schematic: (**a**) Faraday probe 2D Side view, (**b**) 2D front view

Table 1 HET operating conditions - inner magnet current: 4.1 A, Outer Magnet Current: 2.3 A

Pressure (µTorr-Kr)	Bleed Flow Rate (mg/s)	Discharge Voltage (V)	Anode Flow Rate (mg/s)	Cathode Flow Rate (mg/s)	Mean Discharge Current (A)	RMS AC Discharge Current (A)
6.236 ± 0.2	0	300.0	14.14	1.200	20.04	2.181
14.03 ± 0.6	8.571	300.0	14.14	1.200	19.95	1.326
21.83 ± 0.9	22.86	300.0	14.14	1.200	20.22	0.8688
28.06 ± 1.1	34.29	300.0	14.14	1.200	20.44	0.8687
32.74 ± 1.3	40.00	300.0	14.14	1.200	20.65	0.8581
38.98 ± 1.6	54.29	300.0	14.14	1.200	20.92	0.9151

20 A are selected as the H9 thruster is stable at this operating point, with discharge current oscillations less than 10 A in amplitude, 50% of the mean discharge current.

Data collection

The discharge current and ion flux oscillations of the H9 HET are recorded using a Teledyne LeCroy CP150 current probe and a Teledyne Lecroy HVD3106A voltage probe across a resistor, respectively, connected to a HDO6104 Teledyne LeCroy oscilloscope. The current probe was placed immediately downstream from the discharge filter and outside of the vacuum chamber. The uncertainty and bandwidth of the current probe are ± 1% and 10 MHz; for the voltage probe they are ± 1% and 120 MHz; and for the oscilloscope, they are ± 0.5% full scale and 1 GHz. The oscilloscope has 12 bits of resolution, and a sampling rate of 25 MS/s is used over an interval of 20 ms, for 500,000 samples in all. The data has precision to three decimal places, which is sufficient for the eCCM algorithm. This is necessary since the eCCM algorithm requires high-resolution data such that no two points are similar in value for the k-nearest neighbor (KNN) method to operate successfully. The BMO frequency was observed to be 13.85 kHz at a pressure of 6.236 μTorr, which occurs for 277 cycles in the interval. Taking every 30th sample from the dataset gives 60 samples per cycle.

Thruster data is measured after the peak-to-peak discharge current varied within ± 1% of the average, which took approximately two hours. The discharge current steady-state criterion was used for each operating pressure condition to ensure consistency in the data collection process.

eCCM technique, TLPPs, and post-processing of data

eCCM uses the Pearson correlation coefficient, shown in Eq. 1, to quantify the cross-mapping skill that determines how causally linked two signals may be. Positive correlation coefficients closer to one represent strong correlation and causal linkage between two variables, whereas lower values represent weaker correlation and causal linkage. Negative correlation coefficients represent anti-correlation [15]. The technique involves several parameters that were iteratively tuned to determine the appropriate result. These parameters are the time lag, the time shifts, the number of dimensions, which can be determined using Cao's algorithm, the number of points per segment, and the number of segments. Data is broken in half into training and testing sets, using the KNN algorithm. It is important to populate the shadow manifold used in eCCM with enough points for the KNN algorithm to achieve convergence. The manifold reconstruction process prevents false positives from the Pearson correlation coefficient [15]. Minor variations exist in the results obtained from repeated eCCM simulations due to the algorithm's selection of a random segment of points.

$$\rho_{ab} = \frac{\sum(a_i - \bar{a})(b_i - \bar{b})}{\sqrt{\sum(a_i - \bar{a})^2 \sum(b_i - \bar{b})^2}} \tag{1}$$

The eCCM and PDF-TLPP code was implemented in Python. MATLAB is also used to assist in computational tasks such as computing FFTs and as well as performing statistical analyses. The algorithm was run on measurements from each pressure three times, with averages and standard deviations computed to aid in the uncertainty analysis. The statistical nature of the algorithm results in slightly different results between each trial run.

Uncertainty quantification

Systematic and random errors are quantified as part of this study's error analysis. Systematic errors are introduced by discharge current, ion flux, and pressure probe measurements along with the oscilloscope, which are defined in the data collection subsection. The random error includes statistical variance between sequential executions of the eCCM algorithm. The error is quantified in the eCCM part of the results and discussion section. Relevant plots and tables in this paper include uncertainty quantification.

Results and discussion

The results obtained consist of discharge current and ion flux time-domain characteristics in section A, their FFTs in section B, correlation-time shift plots and an overall correlation-operating pressure plot in section C, and PDF-TLPPs and lastly their EMDs in section D. The results were obtained at the six background pressures of 6.236, 14.03, 21.83, 28.06, 32.74, and 38.98 μTorr. These results demonstrate the similarity between discharge current and ion flux in the time and frequency domains, their correlation and causation, and the uniqueness of their TLPPs at each operating pressure.

Time domain representations

Figure 4 shows an example of the discharge current and ion flux in the time domain, as were measured for the lowest operating pressure of 6.236 μTorr and the highest operating pressure of 38.98 μTorr. Both the discharge current and ion flux appear to be a combination of various sinusoids, resulting in different amplitude peaks [11]. It is apparent that the ion flux current strongly resembles the discharge current at the 6.236 μTorr pressure condition and more weakly at the 38.98 μTorr pressure condition, though with noticeable phase shift where the discharge current leads the ion flux, which could indicate that there exists a significant correlation between the two. More information is needed to draw this conclusion, however, as this alone does not uniquely imply a correlation, which is precisely where the eCCM algorithm excels at and can be employed. It is not possible to compare unsynchronized time domain waveforms and waveforms recorded at separate times, but it is possible to compare them in the frequency domain.

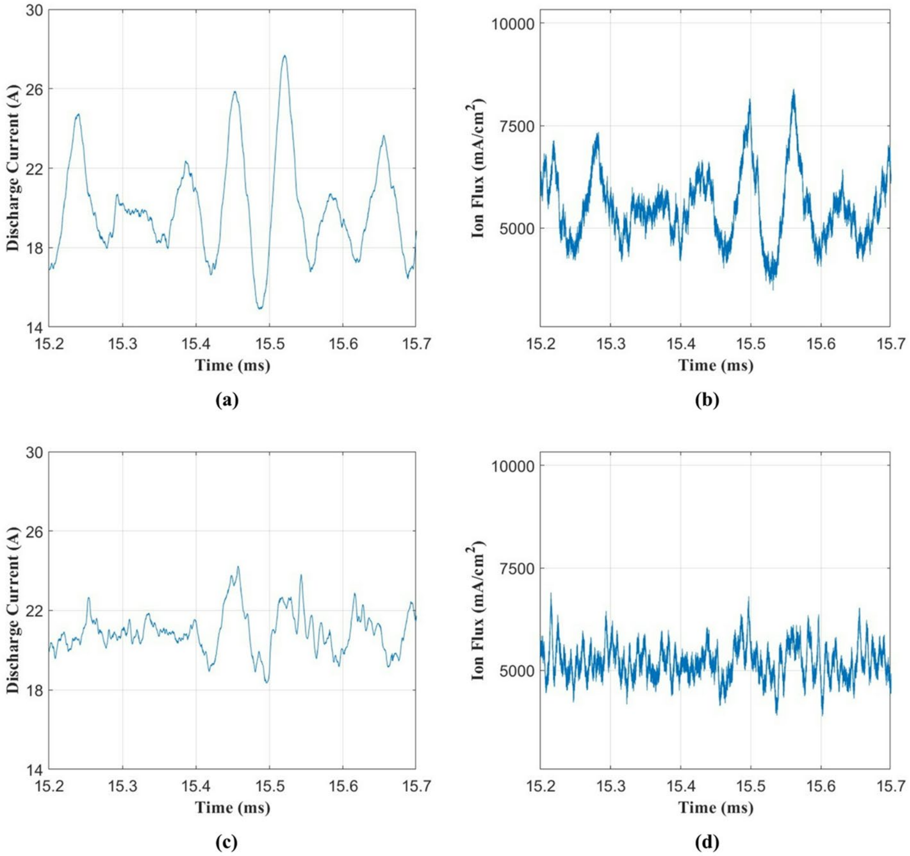

Fig. 4 Discharge current (**a**) and Ion Flux (**b**) as a function of time at 6.236 μTorr and discharge current (**c**) and Ion Flux (**d**) as a function of time at 38.98 μTorr (no bleed flow condition)

Frequency domain representations

It is helpful to look at the discharge current and the ion flux in the frequency domain as similar frequencies may imply a propagating physical effect from the thruster's discharge chamber out to the plume. Figure 5 shows the discharge current and ion flux in the frequency domain, showing at 6.236 μTorr the dominant 13.85 kHz BMO in both signals along with an unknown 10.85 kHz component. As expected, the fast Fourier transforms (FFTs) share the same frequency components and are analogous to the time domain representation. However, at 38.98 μTorr, there is significant difference beyond the first dominant frequency of 11.50 kHz, where additional dominant frequency components arise in the ion flux at 88.85 kHz and 107.1 kHz. This suggests that additional physical mechanisms may be present at higher pressures.

Table 2 shows how the dominant frequencies of the discharge current and ion flux waveforms change with operating pressure at all operating pressures beyond the lowest and highest operating pressures. More than one dominant frequency appears in every ion flux pressure condition, whereas four out of six of the discharge current pressure conditions have just one dominant mode. There is no clear trend on how the discharge current and ion flux dominant frequencies change with background pressure.

Differences were observed in the time domain representations of the discharge current and ion flux due to differences in the frequency content in the signals. This would suggest that the correlation decreases as operating pressure increases. However, time

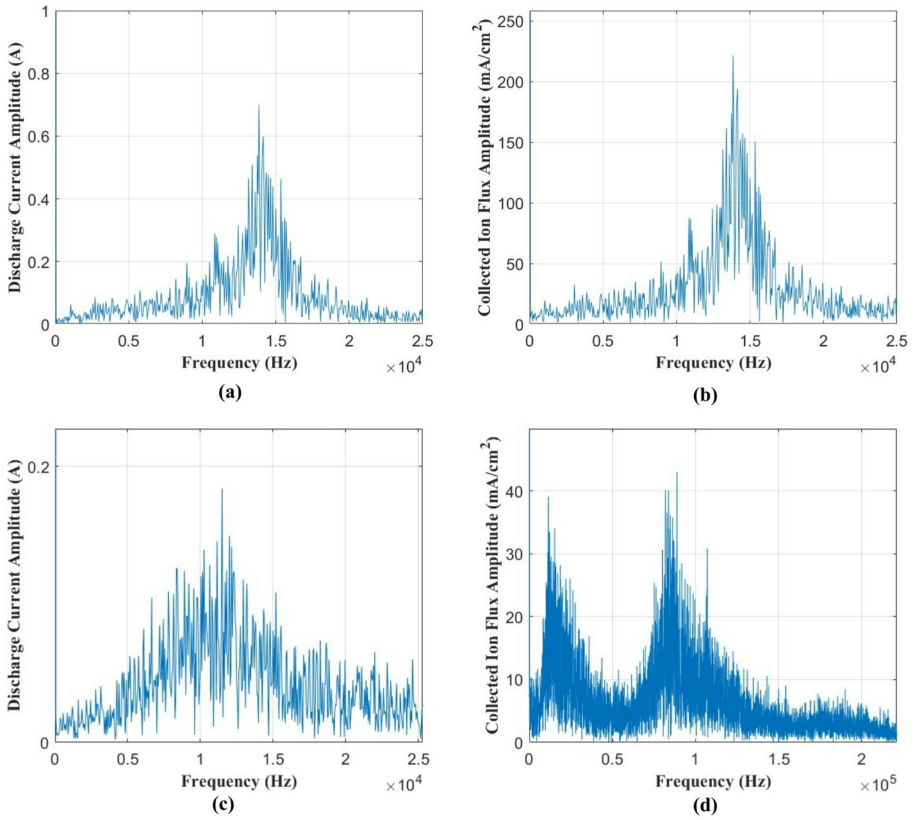

Fig. 5 FFT of discharge current (**a**) and Ion flux (**b**) as a function of frequency at 6.236 µTorr and FFT of discharge current (**c**) and Ion Flux (**d**) as a function of frequency at 38.98 µTorr (no bleed flow condition)

Table 2 Frequency characteristics of discharge current and ion flux

Pressure (µTorr)	Discharge Current Dominant Frequencies (kHz)	Ion Flux Dominant Frequencies (kHz)
6.236 ± 0.2	10.85, 13.85	10.85, 13.85
14.03 ± 0.6	14.65	14.65, 100.0
21.83 ± 0.9	14.15	14.15, 100.0
28.06 ± 1.1	9.600, 17.30, 20.40	17.30, 84.70, 106.6
32.74 ± 1.3	11.60	11.60, 84.70, 107.3
38.98 ± 1.6	11.50	11.50, 88.85, 107.1

domain and frequency domain plots alone are not sufficient to determine correlation; the eCCM algorithm is needed to properly arrive at such a conclusion.

Correlation plots

The output of the eCCM algorithm provides correlation plots between discharge current and ion flux as a function of time shift. Correlation information provides an understanding of how discharge current affects ion flux if at all. After experimenting with the settings of the eCCM algorithm, an optimal set of parameters was identified that helped unpack the information contained within the data. The settings in Table 3 apply to each correlation versus time-shift plot:

Let X represent the discharge current and let Y represent the ion flux henceforth. A time lag of 1 representing one 40-ns time step of the simulation was chosen as there did not appear to be any difference in the output of the eCCM algorithm for higher time

Table 3 eCCM Algorithm Settings

Parameters	
Discharge Current	X
Ion Flux	Y
Time lag	1 (1 time step of simulation, 40 ns)
Time steps	-100 to 101
Dimensions	10
L	1000
N_{it}	8

lags. During experimentation, it was observed that the number of time steps must be large enough so that the time-shifted global correlation peaks could be observed. The number of dimensions allows for a better ability to search for causality in signals X and Y. L, the number of points per segment, needs to be as large as 1000 so that there are enough points on each segment of the manifold. Likewise, N_{it}, the number of segments, must be as large as 8 so that there are multiple segments that represent a total of 8000 points.

Figure 6a suggests that there is a high, positive correlation between discharge current and ion flux. The blue curve representing X causes Y is below the red curve representing Y causes X for negative time shifts. Since the blue curve is also above the red curve for positive time shifts, this means that discharge current influences the ion flux. This agrees with the hypothesis that discharge current and ion flux are correlated, where discharge current causes ion flux. Discharge current consists of ion current, part of which leaves the discharge and goes into the plume as ion flux, which is eventually collected by the Faraday probe. In this case, the discharge current not only causes the ion flux but in a very strong manner as indicated by a high correlation peak value. Dynamically, this means that oscillations have structure that would indicate that the ion flux is derived from the discharge current. The correlation-time shift curves also have sinusoidal shape, which is to be expected for correlated signals that are also causal. The peak correlation for discharge current cross mapping ion flux is 0.9547, which is very strong, positive correlation.

Figure 6b and f also show that discharge current influences ion flux. The waveform global peaks, for discharge current causes ion flux and ion flux causes discharge current, also appear to be getting narrower, as evidenced by the time shift width needed to attain a zero crossing starting from the global correlation peak and moving outwards. A small, negative correlation also appears, which could physically mean that increasing discharge current leads to a smaller ion flux. The global peaks consistently occur at positive time shifts of 30 and negative time shifts of 35, which are tied to the phase differences between the signals. The waveforms also cross each other at a time shift of around 0. This behavior is what is expected when two signals are causal.

At pressures greater than 28.06 μTorr, correlation no longer continues decreasing with increasing pressure. Figure 7 shows that the max correlation tied to the discharge current causing ion flux relationship flattens out in the data range collected. These results could indicate that saturation occurs between discharge current and ion flux dynamics with increasing background pressure.

As expected, the discharge current does indeed appear to influence ion flux. As pressure increases, the correlation between them decreases. Higher operating pressure leads to increased ion scattering through increased charge exchange (CEX) collisions,

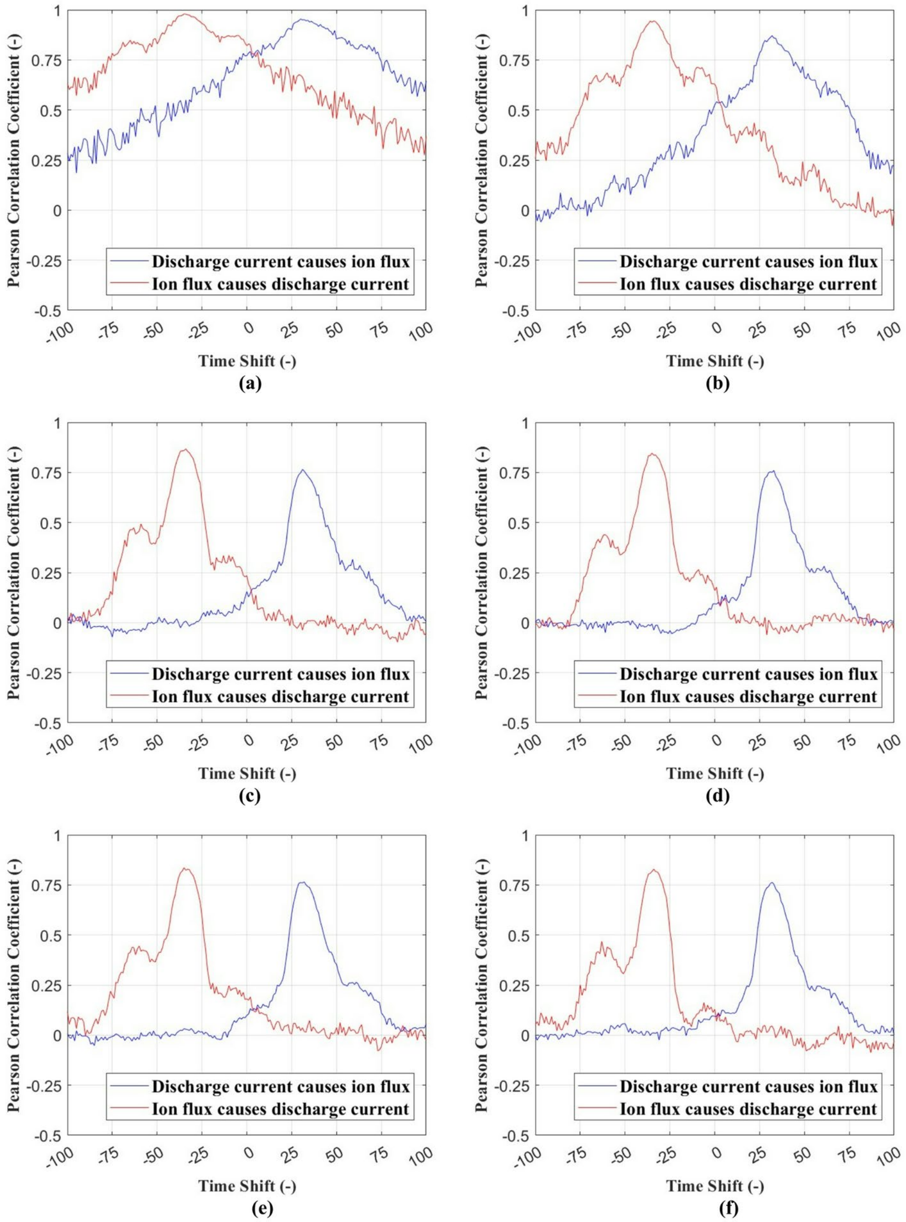

Fig. 6 Pearson correlation coefficient as a function of Time Shift at Plots 6.236 (**a**), 14.03 (**b**), 21.83 (**c**), 28.06 (d), 32.74 (**e**), 38.98 (**f**) μTorr

decreasing the number of ions that strike the Faraday plate, reducing ion flux, and thus lowering correlation. Additionally, the plume divergence angle is known to increase with operating pressure, leading to fewer plume ions striking the collector plate, which corresponds with the shift upstream in the ionization and acceleration regions [20].

Time-lagged PDF phase portrait representations

Phase portraits represent an alternative to a time domain representation of a signal and can make it easier to identify differences between various thruster waveforms. To produce PDF-TLPPs and the following correlation versus time-shift plots, datasets are decimated by taking one of every 30 samples out of 500,000, resulting in 16,666 samples. Table 4 shows the settings that are used to produce the PDF-TLPPs of the discharge

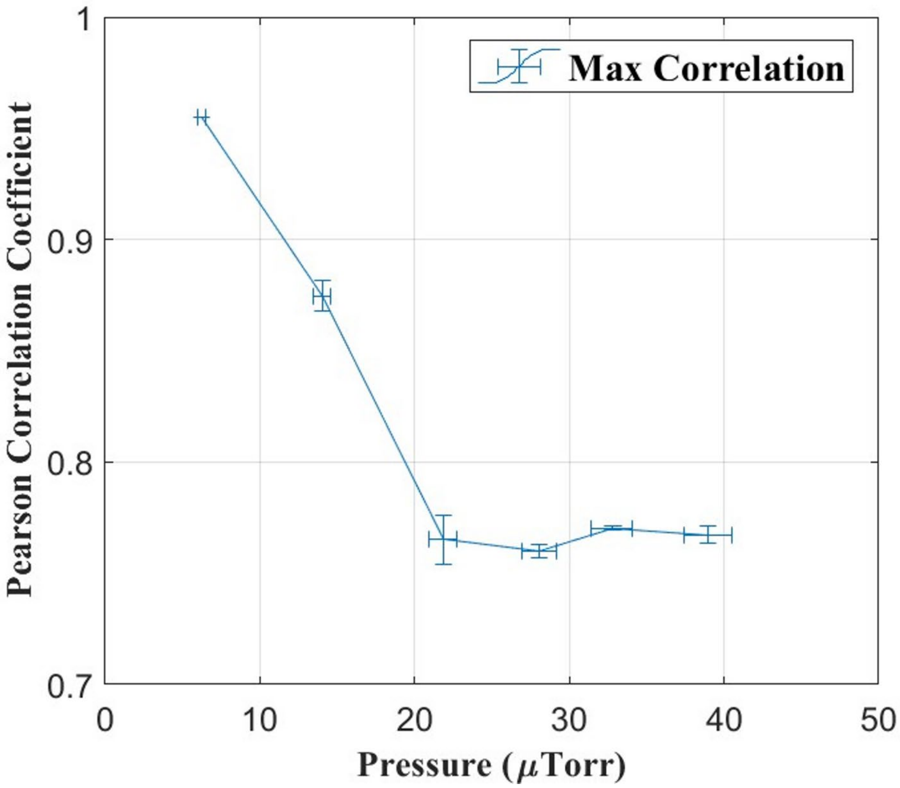

Fig. 7 Pearson correlation coefficient as a function of background pressure

Table 4 TLPP settings

Settings
Time Lag: 1000 (1000 time steps of simulation, 40 μs)
Dimensions: 2
Bins: 30

current and ion flux. TLPPs show a signal in phase space by plotting its output against a time-shifted output. Thus, a time lag of 1,000 is used so that one can distinguish the signal and its shifted version instead of seeing similar values for a smaller shift. Two dimensions are selected to represent the signal and its phased-shifted version, which are to be represented in the TLPP. 30 bins are selected to ensure there would be enough resolution in the color map to prevent low contrast.

Figure 8 (a-f) shows where most of the signals are located, which is at 20 A for the discharge current and 20 mA for the ion flux. The centers of the regions have the highest intensity. The PDF-TLPPs for discharge current and ion flux are observably similar in shape at each pressure condition. As operating pressure increases, the shapes become smaller and more compact. This reduction in oscillation with increasing operating pressure agrees with the results of Snyder et al. [21]. It is important to note that each thruster operating condition produces its unique phase portrait. It is important to further note that changing the time lag does not change the high-intensity central region in the phase portraits at all pressures. The time lag does not have to be chosen to be less than the period of the breathing mode either, since exceeding the breathing mode would

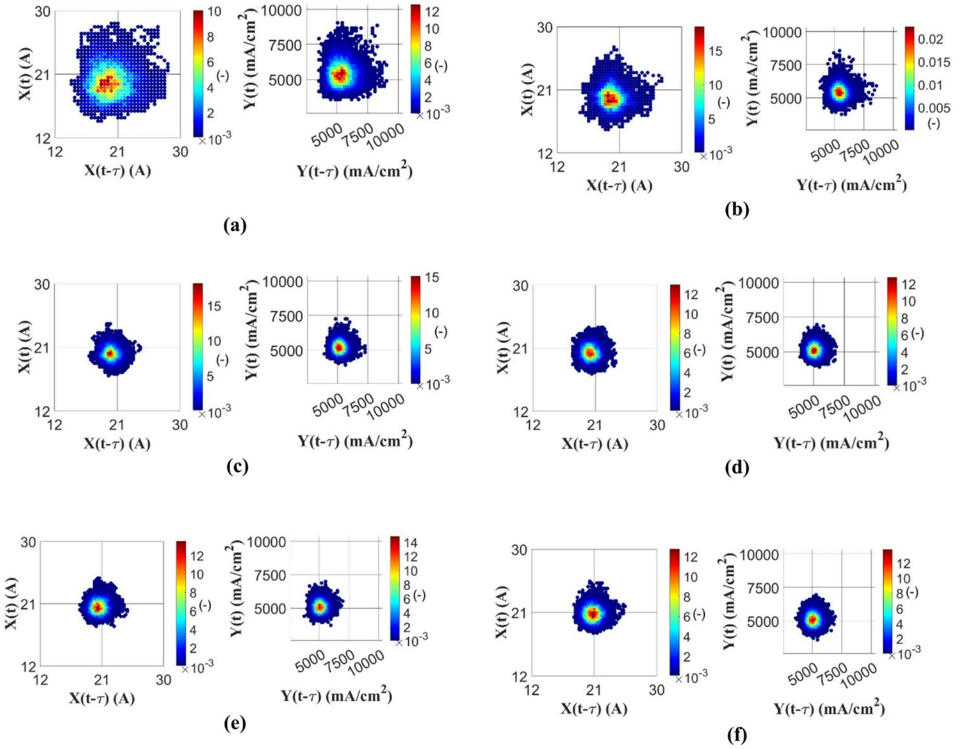

Fig. 8 PDF-TLPPs, discharge current (X) on the left and ion flux (Y) on the right in each cell for **a**, **b**, **c**, **d**, **e**, and **f** at 6.236, 14.03, 21.84, 28.06, 32.74. and 38.98 μTorr, respectively

Table 5 Locations of maximum intensity of TLPPs

Discharge Current TLPP	Intensity	Location (A, A)	Ion Flux TLPP	Intensity	Location (mA/cm^2, mA/cm^2)
Figure 7a	0.0100	(18.7, 19.6)	Figure 7a	0.0128	(5.45×10^3, 5.45×10^3)
Figure 7b	0.0185	(19.4, 19.4)	Figure 7b	0.0226	(5.43×10^3, 5.43×10^3)
Figure 7c	0.0181	(20.0, 20.3)	Figure 7c	0.0151	(5.32×10^3, 5.09×10^3)
Figure 7d	0.0130	(20.5, 20.3)	Figure 7d	0.0128	(5.06×10^3, 5.06×10^3)
Figure 7e	0.0135	(20.6, 20.2)	Figure 7e	0.0148	(5.06×10^3, 5.06×10^3)
Figure 7f	0.0128	(21.1, 20.6)	Figure 7f	0.0138	(5.22×10^3, 5.12×10^3)

just move the shifted signal to the next cycle of the breathing mode. The time lag does change the shape of the plots and the EMD, as expected.

Table 5 presents additional numerical information about the salient features of the phase portraits in Fig. 8, specifically the highest intensity points and their locations. We argue that each phase portrait will have a unique point of highest intensity. This unique feature allows one to distinguish one phase portrait from another and provides an effective means to represent thruster operation. We will continue to discuss important features and metrics that can be used to analyze TLPPs in the following paragraphs. These features could also be used as a part of a machine learning framework to predict the operational state of a HET.

Though we only report the location of the highest intensity point and its corresponding intensity, we propose a complete set of salient features that also includes the minimum, the maximum, average, and standard deviation of the currents in each axis, the area of each colored intensity region, the total area of the phase portrait, the shape of

Table 6 EMD of each pair of TLPPs from each operating pressure

Pressure (μTorr)	**6.236**	**14.03**	**21.84**	**28.06**	**32.74**	**38.98**
6.236	0	1.092	1.672	1.753	1.871	2.023
14.03	1.092	0	0.7046	0.9108	1.165	1.477
21.84	1.672	0.7046	0	0.3199	0.6148	1.001
28.06	1.753	0.9108	0.3199	0	0.3134	0.6966
32.74	1.871	1.165	0.6148	0.3134	0	0.4008
38.98	2.023	1.477	1.001	0.6966	0.4008	0

each colored intensity region, and the shape of the phase portrait and its outliers. Additionally, a metric known as the Earth mover's distance (EMD) can be used to represent the degree of similarity between two phase portraits, combining all of the aforementioned features into one single feature. The EMD represents how much matter must be moved to make one object equivalent to another. Table 6 shows a symmetric and hollow matrix that represents the EMD between the phase portraits of the discharge current at each operating pressure. The EMD matrix shows that the EMD increases with increasing operating pressure when the lowest pressure is taken as the reference TLPP. This can be observed visually from Fig. 7 where the TLPP area decreases with increasing operating pressure, which means there is more Earth to move to attain the same phase portrait. A reference phase portrait allows one to discern between phase portraits using the EMD metric.

These features altogether allow one to uniquely identify a phase portrait. They allow one to determine what pressure a phase portrait is tied to and whether that phase portrait represents where pressure facility effects are not relevant. This occurs as background pressure approaches the vacuum pressure of space, where the discharge current oscillation amplitude reaches a certain level and stops changing with operating pressure.

Conclusion

This study uses the eCCM algorithm to determine the correlation and causation between discharge current and ion flux in a HET at various operating pressures. We have shown that, with proper tuning and selection of optimal parameters, the eCCM technique can successfully determine causality between discharge current and ion flux in a HET at various operating pressures. The ability of the eCCM technique to uncover physical information contained within discharge current and ion flux provides more confidence in its applicability to other HET signals. Some examples include other plasma parameter measurements in the discharge and in the plume. Information about the edges of the vacuum chamber and behind the thruster can also be sampled and analyzed using the eCCM technique. Parameters other than operating pressure can also be swept to understand their relationships with correlation and causation. The eCCM technique serves as an additional benchmark for datasets, where known results can be coupled with the eCCM output for validation purposes.

Time domain and frequency domain representations are difficult to manipulate when trying to observe their changes with respect to varying operating pressures. The phase portraits we show allow for an improved, compact, and more easily accessible representation of signals such as discharge current and ion flux. Particularly, TLPPs allow one to observe when a thruster is in a certain operational mode. Time domain characteristics such as average discharge current and peak-to-peak discharge current, and frequency domain characteristics such as dominant frequencies in the FFT, change with operating pressure. We show that the EMD is a concise metric that can also be used to quantify the difference between two TLPPs. Any combination of these approaches and metrics can be used to fully describe a TLPP for classification and recognition purposes. Phase portraits encapsulate these changes and show whether a thruster behaves differently between facilities or between ground and space.

Nomenclature

JPL	Jet Propulsion Laboratory
L	number of points per segment
eCCM	extended Convergent Cross Mapping
HET	Hall Effect Thruster
TLPP	Time-Lagged Phase Portrait
EMD	Earth Mover's Distance
CCM	Convergent Cross Mapping
HPEPL	High Power Electric Propulsion Laboratory
BMO	Breathing Mode Oscillations
AFRL	Air Force Research Laboratory
MFC	Mass Flow Controller
PDF	Probability Density Function
FFT	Fast Fourier Transform
KNN	K-Nearest Neighbor
CEX	Charge Exchange

Acknowledgements
The authors would like to thank the AFRL, particularly Dr. Cesar Huerta Canales, Dr. Justin Koo, and Dr. Christine Greve, for allowing us to develop our code based on their eCCM and phase portrait implementations. This study would not have been possible without their invaluable explanations and insights.

Author contributions

A. Krishnan executed the study and wrote the paper. N. Butler-Craig assisted with experimentation and paper writing. D. Lev provided technical guidance. M. Walker provided technical guidance.

Funding
No funding was received for conducting this study.

Data availability

N/A.

Code availability

N/A.

Declarations

Competing interests

The authors declare no competing interests.

Received: 29 July 2025 / Accepted: 8 March 2026

References

1. Bapat A, Salunkhe PB, Patil AV (2022) Hall-effect thrusters for deep-space missions: a review. IEEE Trans Plasma Sci 50:189–202
2. Goebel DM, Katz I, Mikellides IG (2023) Fundamentals of electric propulsion. Wiley
3. Byers D, Dankanich JW (Sep 2009) A review of facility effects on Hall effect thrusters. In: IEPC-2009-076, 31st International Electric Propulsion Conference.. In: IEPC-2009-076, 31st
4. Dankanich JW, Walker MLR, Swiatek MW, Yim JT (May 2017) Recommended practice for pressure measurement and calculation of effective pumping speed in electric propulsion testing. J Propul Power 33:668–680
5. Frieman JD, King ST, Walker MLR, Khayms V, King D (2014) Role of a conducting vacuum chamber in the Hall effect thruster electrical circuit. J Propul Power 30(Nov):1471–1479
6. Walker JA, Langendorf SJ, Walker MLR, Khayms V, King D, Peterson P (Nov 2016) Electrical facility effects on hall current thrusters: electron termination pathway manipulation. J Propuls Power 32:1365–1377
7. Byrne MP, Roberts PJ, Jorns BA (Jun 2022) Coupling of electrical and pressure facility effects in Hall effect thruster testing. In: 37th International Electric Propulsion Conference, IEPC-2022-377
8. Choueiri EY (2001) Plasma oscillations in hall thrusters. Phys Plasmas. 8:1411–1426
9. Fife J, Martinez-Sanchez M, Szabo J (Jul 1997) A numerical study of low-frequency discharge oscillations in hall thrusters. In: 33rd Joint Propulsion Conference and Exhibit, AIAA 1997–3052

10. Leporini L, Giannetti V, Saravia MM, Califano F, Camarri S, Andreussi T (Aug 2022) On the onset of breathing mode in hall thrusters and the role of electron mobility fluctuations. Front Physics 10
11. Walker MLR, Victor AL, Hofer RR, Gallimore AD (May 2005) Effect of backpressure on ion current density measurements in hall thruster plumes. J Propul Power 21:408–415
12. Brown DL, Walker MLR, Szabo J, Huang W, Foster JE (May 2017) Recommended practice for use of Faraday probes in electric propulsion testing. J Propul Power 33:582–613
13. Piragino A, Faraji F, Reza M, Ferrato E, Piraino A, Andreussi T (Mar 2021) Background pressure effects on the performance of a 20 kW magnetically shielded hall thruster operating in various configurations. Aerospace 8:69
14. Diamant K, Spektor R, Beiting E, Young J and Curtiss T (Jul 2012) The effects of background pressure on hall thruster operation,". In: 48th AIAA/ASME/SAE/ASEE Joint Propulsion Conference, AIAA 2012-3735.
15. Huerta CE, Martin RS, Eckhardt DQ, Koo JW (Jul 2021) Determining causality in hall effect thrusters using extended convergent cross mapping, part I. Plasma Sources Sci Technol 30:075004
16. Huerta CE, Martin RS, Eckhardt DQ, Koo JW (Mar 2022) Determining causality in hall effect thrusters using extended convergent cross mapping: II. Plasma Sources Sci Technol. 31:035015
17. Greve CM, Hara K, Martin RS (Aug 2022) Data-driven modeling for nonlinear dynamics of physical phenomena in Hall Effect Thrusters. Front Phys. 10
18. Hofer RR, Cusson SE, Lobbia RB, Gallimore AD (Oct 2017) The H9 magnetically shielded Hall thruster. In: 35th International Electric Propulsion Conference, IEPC-2017-232.
19. Su LL, Vazsonyi AR, Jorns B (Aug 2020) Performance of a 9-kW magnetically-shielded Hall thruster with krypton. In: AIAA Propulsion and Energy 2020 Forum, AIAA 2020–3617.
20. Kerber TV, Baird MJ, McGee-Sinclair RF, Lemmer KM (Sep 2019) Background pressure effects on plume properties of a low-cost Hall effect thruster. In: 36th International Electric Propulsion Conference, IEPC-2019-513.
21. Snyder JS, Lenguito G, Frieman JD, Haag TW, Mackey JA (Jul 2012) The effects of background pressure on SPT-140 thruster performance at multiple power levels. In: 48th AIAA/ASME/SAE/ASEE Joint Propulsion Conference, AIAA 2018-XXXX.

Publisher's note